

Physics-Informed Ensemble Representation for Light-Field Image Super-Resolution

Manchang Jin[†], Gaosheng Liu[†], Kunshu Hu, Xin Luo, Kun Li, *Member, IEEE*, Jingyu Yang, *Senior Member, IEEE*

Abstract—Recent learning-based approaches have achieved significant progress in light field (LF) image super-resolution (SR) by exploring convolution-based or transformer-based network structures. However, LF imaging has many intrinsic physical priors that have not been fully exploited. In this paper, we analyze the coordinate transformation of the LF imaging process to reveal the geometric relationship in the LF images. Based on such geometric priors, we introduce a new LF subspace of virtual-slit images (VSI) that provide sub-pixel information complementary to sub-aperture images. To leverage the abundant correlation across the four-dimensional data with manageable complexity, we propose learning ensemble representation of all C_4^2 LF subspaces for more effective feature extraction. To super-resolve image structures from undersampled LF data, we propose a geometry-aware decoder, named *EPIXformer*, which constrains the transformer’s operational searching regions with a LF physical prior. Experimental results on both spatial and angular SR tasks demonstrate that the proposed method outperforms other state-of-the-art schemes, especially in handling various disparities. Our codes are available at <https://github.com/kimchange/PILF>.

Index Terms—Light field image processing, feature representation, super resolution, transformer, physical modelling.

I. INTRODUCTION

LIGHT field (LF) imaging can capture both the intensities and directions of light rays that pass through a scene. Compared with conventional 2D imaging, it provides rich geometric information for scene understanding and consequently enables a variety of applications such as semantic segmentation [1], depth estimation [2], 3D rendering [3], object detection [4] and so on. However, LF imaging suffers from an intrinsic tradeoff between spatial and angular resolutions when encoding the 4D structure into a 2D sensor due to the limited resolution of imaging sensors. To handle the resolution dilemma, developing computational algorithms to enhance the spatial and angular resolutions is drawing increasing attentions. In the literature, two principal tasks are introduced to address the problem: spatial super-resolution (LFSSR) and angular super-resolution (LFASR). One key in common is incorporating the 4D LF structural prior into the method design.

The traditional optimization-based methods designed for LF super-resolution exploited non-local information to recover

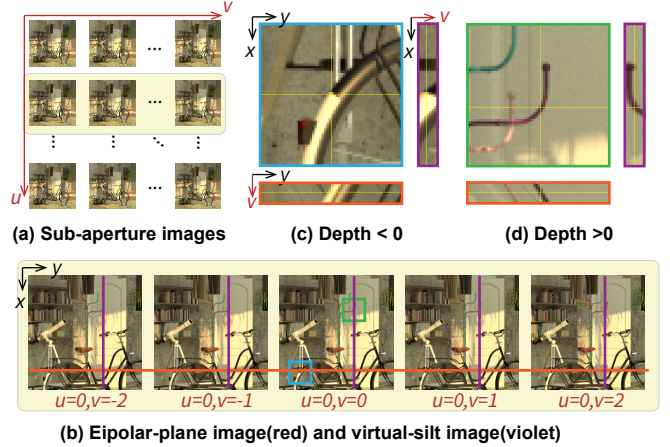


Fig. 1. An illustration of VSI formation: (a) SAIs, each image represents observation from a different angle. (b) One row of SAIs, the red line selects one horizontal EPI and the violet line selects one vertical VSI, note that this selection is just for illustration and not unique. Then we zoom in the blue region (c) where depth < 0 and the green region (d) where depth > 0 . Note that all sub-images in (c) and (d) are shown in the *same* scale factor. We can find that VSI can produce cognizable image with a different sampling factor, which can be interpreted as observing the scene from a virtual slit thus may contain sub-pixel information compared to SAI.

the LF, such as LFBM5D [5], whose PSNR improved about 2dB than bicubic interpolation. Benefiting from the success of convolutional neural networks (CNNs), the learning-based methods for LFSR have made significant progress in reconstructing the high-resolution (HR) LFs from low-resolution (LR) observations. Learning-based method RCAN outperforms LFBM5D without considering the light-field structural prior, which implies great potential for learning-based LF super-resolution approaches. Among them, various modules have been introduced to utilize domain-specific 2D convolutions to extract the structure prior from 4D LF data. For example, spatial-angular alternating convolution [6], spatial-angular versatile convolution [7], and disentangling mechanism [8]. In summary, these methods consider performing convolutions on the subset of three well-known 2D representations of LF images, *i.e.*, sub-aperture images (SAIs), macro-pixel images (MacPIs), and epipolar-plane images (EPIs), which are experimentally effective in terms of their reported results. However, based on the analysis of the coordinate transformation of the LF imaging process, we found that LF imaging is essentially a 4D imaging with significant 2D constraints (see Section III), and there still exists other important priors that can directly constrain the network design and regularize the training. And based on this observation, we re-organize LF image into a new

This work was supported in part by the National Natural Science Foundation of China under Grant 62231018 and Grant 62171317. (*Corresponding author: Jingyu Yang*)

M. Jin, G. Liu, K. Hu, X. Luo, and J. Yang are with the School of Electrical and Information Engineering, Tianjin University, Tianjin 300072, China.

Kun Li is with the College of Intelligence and Computing, Tianjin University, Tianjin 300350, China.

[†]These authors contributed equally to this work.

cognizable 2D representation, termed as virtual-slit images (VSIs), as illustrated in Fig. 1 (c) and (d). The VSI can be regarded as observing the scene from a single slit, which provides a new perspective to represent an LF and can contain rich sub-pixel information at that specific line position. More analyses of VSI can be found in section III-B.

Based on these observations, we leverage the SAI, MacPI, EPI, and VSI representations and consequently propose a C_4^2 feature extractor (C_4^2 FE) to fully exploit the structure prior of LF images. The C_4^2 FE also unifies previous modules for LF feature extraction by complementing the VSI feature extraction into our unified design to make it a complete set. And since C_4^2 is designed as a generic extractor for all tasks that fulfill “4D data with 2D priors”, we further designed a LF specialized, transformer-based architecture, EPIXformer as a context-aware decoder, which is constrained according to the LF imaging character to further enhance the capability to handle large disparities.

We apply the C_4^2 FE and EPIXformer on both LFSSR and LFASR tasks, 2 well-known LF challenges to prove the effectiveness of our design. Experimental results show that our methods achieved better visual and quantitative results than previous studies.

Our main contributions are as follows:

- We analyzed the coordinate transformation to reveal geometric correlation in LF imaging, and introduce a new LF subspace of virtual-slit images (VSI) that provide sub-pixel information complementary to sub-aperture images. Based on this analysis, we propose learning ensemble representations derived from C_4^2 LF subspaces to exploit the abundant correlation across the 4D data.
- We propose a geometry-aware decoder, named *EPIXformer*, that constrains the transformer’s operational searching regions by the geometric trajectories of the scene’s LF projection. This facilitates robust recovery of image structures from undersampled LF data with various disparities.
- Compared with state-of-the-art methods, extensive experimental results demonstrate that our method outperforms other methods in terms of quantitative and visual performance on public datasets for both LFSSR and LFASR tasks, verifying the effectiveness of the proposed physics-informed learning framework for LF images.

II. RELATED WORK

This section briefly reviews the related studies on LF spatial and angular SR.

A. LF Spatial SR

The LFSSR aims at generating high-resolution (HR) LF images from their low-resolution (LR) counterparts. Previous methods for LFSSR can be broadly categorized into optimization-based and learning-based approaches.

Optimization-based approaches typically leverage disparity information as priors to aid the SR process. For example, Bishop *et al.* [9] utilized a variational Bayesian framework to reconstruct the scene disparity for LFSSR. Wanner *et al.* [10]

initially estimated disparity maps using EPIs, then utilized them to generate HR images. Mitra *et al.* [11] proposed to process LF patches using a Gaussian mixture model based on disparity values. Rossi *et al.* [12] introduced a graph-based regularizer that enforces the LF geometric structure, enabling the utilization of complementary information across different views for LFSSR. However, these methods heavily rely on accurate depth or disparity information, which can easily lead to unsatisfactory results due to inaccurate estimations.

In recent years, learning-based methods have been introduced for LFSSR [6, 8, 13–19] driven by the CNNs. Yoon *et al.* [6] proposed the pioneer method to simultaneously achieve angular and spatial super-resolution. Yuan *et al.* [13] first employed a single-image SR method on each SAI and then developed a deep EPI-based neural network to further reconstruct the geometric structure of LF. Cheng *et al.* [17] utilized internal and external view similarities using a CNN, Mo *et al.* [18] further used an attention strategy to enhance the performance. Yeung *et al.* [14] utilized spatial-angular separable convolutions instead of 4D convolution to save memory and computational costs, which can efficiently extract spatial and angular joint features. Zhou *et al.* [19] combined the depth defocus information into a CNN-based network. Wang *et al.* [15] proposed LF-InterNet to progressively interact spatial and angular features. Later, they further designed disentangling mechanism [8] to extract four domain-specific features for LFSSR. Jin *et al.* [16] developed LF-ATO, which first adopted an all-to-one strategy for SR and then utilized structure regularization to refine the result. Liang *et al.* [20, 21] used transformer on spatial, angular and EPI domain to deal with LF iamges with large disparity. These methods provide important examples to incorporate observations into network design. Since structure determines function, all observations can be reflected on the physical imaging process, thus the performance can be further improved by incorporating physical priors.

B. LF Angular SR

The LFASR aims at synthesizing novel SAIs from given views, enriching the angular information of LF images. Previous works for LFASR could generally be categorized into depth-based and non-depth-based methods.

Depth-based methods synthesize novel views with the help of disparity estimation. Pearson *et al.* [22] used plenoptic sampling theory as guidance to obtain layer-based geometric information of objects, which helps to synthesize novel views at arbitrary angular positions. Wanner *et al.* [10] used EPI analysis with convex optimization techniques to estimate subpixel-level disparity maps, then calculate the warping maps required for novel view synthesis. Kalantari *et al.* [23] first used CNNs to estimate disparity maps and synthesize new SAIs. Jin *et al.* [24] used a disparity estimator with a large receptive field to estimate depth maps with a blending strategy to refine the results. Jin *et al.* [25] also proposed to construct plane-sweep volumes (PSVs) to achieve more accurate estimation. Ko *et al.* [26] proposed an adaptive feature remixing method to realize angular SR. The depth-based methods require extra

costs to estimate the disparity, and the ASR accuracy often relies much on disparity accuracy.

For non-depth-based methods, Vagharshakyan *et al.* [27] used shearlet transform to provide a sparse representation of the EPIs for LF reconstruction. Wu *et al.* [28] trained CNNs to select sheared EPI patches and fused sheared EPIs to reconstruct high-angular-resolution LF images. Yeung *et al.* [29] reconstructed a densely-sampled LF from a sparsely-sampled LF by alternating convolutions on spatial and angular dimensions. Wu *et al.* [30] designed a deep learning pipeline to handle the aliasing, similar to the conventional Fourier reconstruction filter. Later they proposed a spatial-angular attention network, SAA-Net [31] to cope with non-Lambertian surface and large disparity. Sheng *et al.* [32] used a recurrence-based method to recover the angular resolution. Wang *et al.* [8] proposed DistgASR, using SAIs, MacPIs and EPIs subspace to disentangle LF features. Liu *et al.* [33] achieved ASR by using MacPIs upsampling, which provides an efficient structure to recover the angular resolution. These non-disparity-based methods struggle to handle LFs with large disparity.

III. MOTIVATION

A. 4D LF Optical Imaging

The forward LF imaging model can be formulated as the following linear model.

$$I(x, y, u, v) = \int S(x, y, z) * h(u, v, x, y, z) dz, \quad (1)$$

where $*$ is the 2D convolution operated on dimension (x, y) , it means the 4D LF image I is the convolution of the 3D scene S and the 5D point spread function (PSF) h , and coordinate indices include: u and v for two angular dimensions, x and y for two lateral dimensions, and z for the axial dimension.

Through the imaging formation (1), the characteristics of LF images not only depend on the latent scene content but are also highly modulated by the system's PSF. We first exploit structures of LF PSF to inspire the design of efficient feature extraction for 4D LF images. And geometric-optics dominate the scenes where pixel size is far greater than the wavelength of visible light, thus like [34], we simplify the LF PSF into a delta function to focus on the sampling coordinates from the real-world to the imaging plane for each angle. Assuming Lambertian surface and leaving out out-of-focus blurring, and based on the geometry analysis of Fig 2, the LF PSF can be approximated as

$$\hat{h}(u, v, x, y, z) = s^2(z) \delta(s(z)x - uz/z_0, s(z)y - vz/z_0), \quad (2)$$

where δ is the delta function. Define the origin of z axis by its intersection with the focused plane. Denote by z_0 the focus distance between the camera and the focused plane, at which the disparity is 0. Then, $s(z) = 1 + z/z_0$ is the scaling factor depending on the object position relative to the focused plane. Angular coordinates (u, v) control the disparity based on axial position z . The center position is defined as the origin of the 4D LF coordinates u, v, x, y . The world coordinate of the camera position is $(0, 0, -z_0)$, and $z \in [-z_0, +\infty)$. As a result, the LF imaging can be simplified as

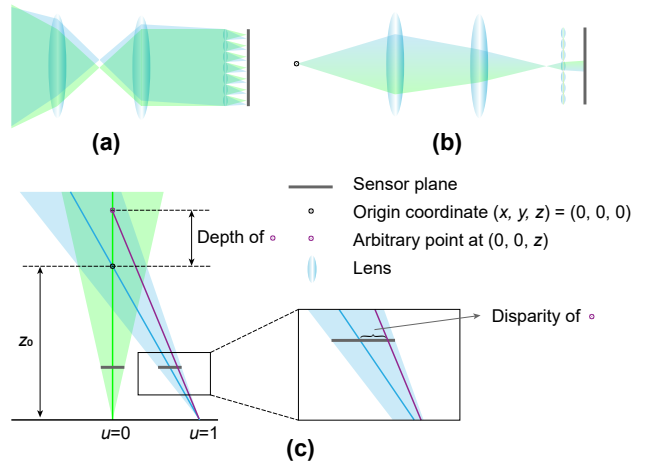


Fig. 2. The analysis of LF imaging, the blue or green color represents the light path of 2 different angles. (a) The light beam path of SAI. (b) The light beam path of MacPI. (c) The coordinate mapping from real-world space to image space.

$$\begin{aligned} \hat{I}(x, y, u, v) &= \int S(x, y, z) * \hat{h}(u, v, x, y, z) dz \\ &= \int S(s(z)x - uz/z_0, s(z)y - vz/z_0, z) dz, \end{aligned} \quad (3)$$

B. C_4^2 2D Subspaces of 4D LF images

From Eq. (3), the coordinate transformation and the projection along the z dimension multiplex 3D information of scene S into the 4D LF space, which indicates that the four dimensions of the LF space are highly correlated. Since u, v, x, y only occupy the first and second dimensions of scene S , we think that 2D constraints are dominant. On the other hand, directly exploiting the four-dimensional (4D) correlation would impose intensive computational and memory demands. Instead, following the divide-and-conquer philosophy, previous approaches turns to exploit correlation of 2D subspaces [6], e.g., the x - y SAI domain [6], u - v MacPI domain [15], and u - x and v - y EPI domains [8]. Note that, among the $C_4^2 = 6$ subspaces, previous works seldom explored the u - y and v - x domains, which might miss prominent LF priors.

Fig. 1 visualizes three 2D subspace images of an LF image: SAIs, EPIs, and VSIs on the x - y , v - y , v - x domains, respectively. The characteristics of SAIs and EPIs have been recognized early on: SAIs are images observed at different angles, while EPIs are linear patterns with depth-related slopes. Note that u - y (v - x) images are stacks of co-located SAI rows (columns) along the orthogonal direction in the angular domain, which are essentially images captured by tilting a virtual line camera around a virtual slit at a different depth. Therefore, we named them as *virtual slit images* (VSI). Hence, intuitively, a VSI contains similar image structures to the associated local region of the SAI. According to the coordinate transformation in the imaging model (3), the pixel sampling stride along the horizontal lateral dimension of the

x - y SAI is $s(z)$, while that of the x - v VSI is $-z/z_0$. The x - v (u - y) VSIs have different sampling rates from the x - y SAIs for the horizontal (vertical) lateral dimension. Therefore, with different sampling rates, VSIs can provide sub-pixel information complementary to SAIs. If an object is at depth z_{vsi} , then its VSI sampling rate is the same to SAI sampling rate at depth z_{sai} , to see the relationship, let $s(z_{\text{sai}}) = -z_{\text{vsi}}/z_0$, and we have

$$z_{\text{sai}} = -z_{\text{vsi}} - z_0. \quad (4)$$

Eq. (4) indicates that VSIs are equivalent to monocular imaging by moving the object of depth z_{vsi} to a new depth z_{sai} . For example, when observing an object at $z = 0$, VSI is equivalent to monocular imaging by moving the object to $z = -z_0$, at which it would ideally have an infinite sampling rate.

The distance between the camera at $-z_0$ and the object at z_{sai} is $z_{\text{sai}} - (-z_0) = -z_{\text{vsi}}$, which means that for an object at z_{vsi} , we can also treat its VSI to be the reversed observation of a virtual silt at $z = 0$. We can also see it from Fig 2 (c), a green line and the blue line will be two adjacent lines on DPI and they converge on the same line at depth $z = 0$, which is the position of virtual silt described above.

Based on the above analysis, with depth-dependent sampling rates, the proposed VSI representation contains much sub-pixel information relative to the SAI subspace, especially when the disparity is relatively small, so leveraging the VSI information would benefit the processing of LF images. For the 4D LF image space, there are six (C_4^2) subspaces in total: two for VSI, two for EPI, one for SAI and the rest one for MacPI, respectively. In this work, we propose learning ensemble representation of all C_4^2 LF subspaces, termed C_4^2 LF representation for short hereafter, to extract LF features more thoroughly.

IV. C_4^2 LF FEATURE EXTRACTOR AND EPIXFORMER

Based on the analysis in Section III, we designed two main components, namely C_4^2 feature extractor and EPIXformer, for LF feature extraction and decoding. We apply the proposed modules for both LFSSR and ASR tasks. In what follows, we describe the design and structure of the two modules.

A. C_4^2 LF Feature Extractor

Previous studies have demonstrated the power of CNNs in the representation and processing of 4D LF images, and 2D convolutions with elaborated network structures can outperform the straightforward 4D convolutions [8]. Based on the above analysis, we design a backbone network for efficient feature extraction to learn the ensemble representation of C_4^2 LF subspaces, including x - y SAI (spatial), u - v MacPI (angular), x - u EPI (vertical), v - y EPI (horizontal), x - v VSI (vertical), y - u VSI (horizontal).

Different from disentangling block [35], which utilizes domain-specific convolutions to first downsample the MacPI and EPI features into subspace and then upsample them into the original size, we adopt fully convolutional layers to equivalently realize these modules. Fig. 3 (c) illustrates how the convolution kernel operates on the input to extract features

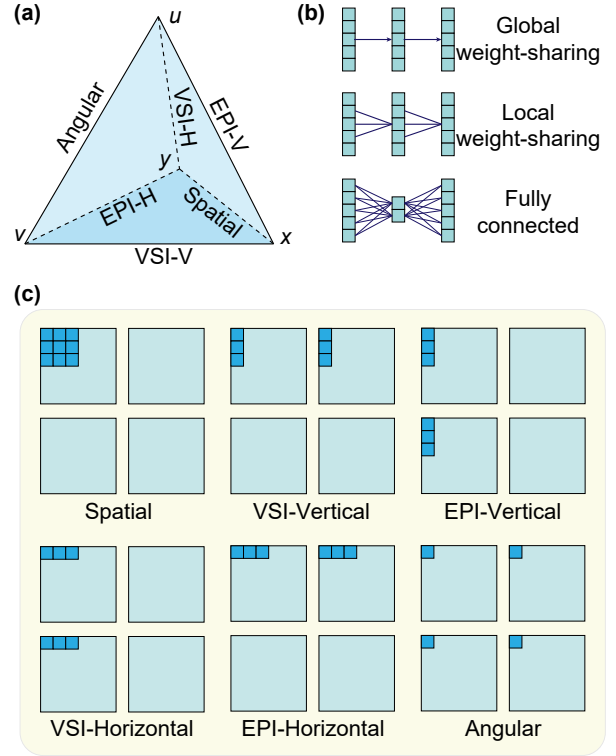


Fig. 3. An illustration of the proposed C_4^2 feature extractor: (a) C_4^2 feature extractor chooses 2 dimensions at a time from 4 LF dimensions u, v, h, w . (b) Global weight-sharing is applied on unchosen dimensions. For chosen dimensions, depending on the dimension's element number, local weight-sharing is applied on chosen spatial dimensions h, w , and chosen angular dimensions u, v are fully connected. (c) The resulting C_4^2 feature extractor appears on LF SAIs in a convolutional layer form, for illustration.

from the corresponding subspace. Based on these subspace-specific convolutions, as shown in Fig. 5 (b), we design a feature extraction module, named C_4^2 Conv block, to learn the ensemble of C_4^2 subspace representation. In this module, the feature maps generated by subspace-specific convolutions are activated by two LeakyReLUs separated by a 1×1 convolution, and followed by a channel to angle (C2A) rearrangement, if necessary, so that the output features of each extractor have the same shape. Then, the features from the six branches are concatenated and fused by the cascading of 1×1 convolution, a Leaky ReLU activation, and a 3×3 convolution. In the C_4^2 Conv block, residual learning is applied by using a local skip connection.

B. EPIXformer as a Geometry-Aware Decoder

Some previous LFSSR methods achieved promising performance by using transformers on spatial, angular, or EPIs [20, 21] domains to exploit non-local information. As a departure, in this work, we design the transformer with the geometric structures of LF imaging. The basic observation is that, given an undersampling LF configuration, a 3D point missed in some angles might be sampled in others due to the disparities among SAIs, and pixels to be super-resolved can be predicted by the sampled counterparts from neighbouring angles with geometric priors.

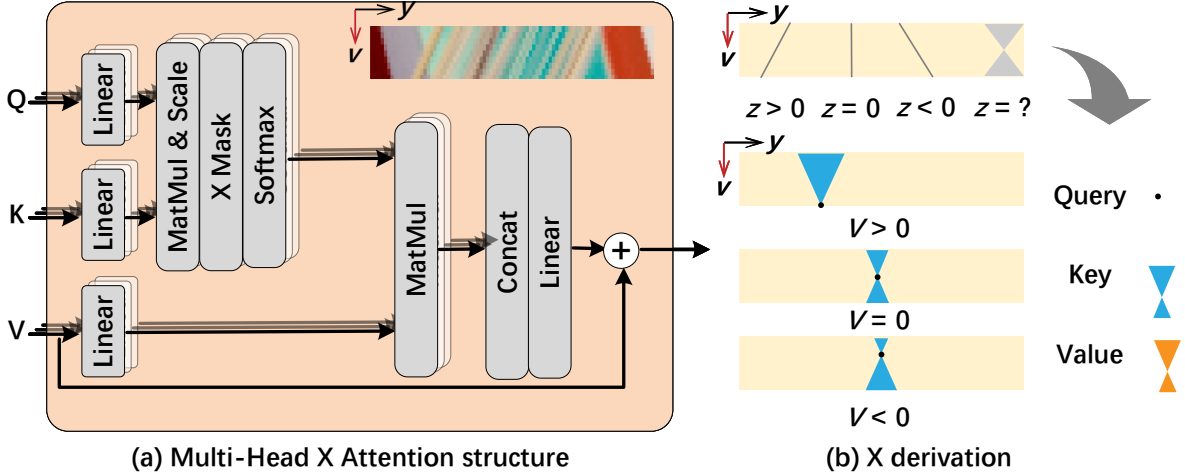


Fig. 4. Structure for proposed MHXA: (a) An EPI from a LF image (b) Image function without occlusions using our equation, showing that when depth is unknown in advance, all possible lines on EPI make an 'X' shape, which determines the designed search window of Query to Key. We listed several 'X' shape of Query at different locations.

As analyzed in Sec. III, LF images have multiple domain-specific representations, and we should select the one where LF geometric characteristics can be well captured by the transformer framework. As indicated in Eq. (3), of the six subspaces, the u - x or v , y dimensions of the EPI subspaces are multiplexed in the same dimension of the latent scene. Thus, there are many pixels that capture the same physical position in the EPIs. Therefore, we operate transformers on the EPI representation similar to [21]. Specifically, consider an x - u EPI at particular \bar{v} and \bar{y} , LF pixels observing an unoccluded 3d point (x', y', z') of the latent scene S are determined

$$u = ((z' + z_0)x - z_0x') / z'. \quad (5)$$

Similarly, the observed pixels in an v - y EPI at particular \bar{x} and \bar{u} are given by $v = ((z' + z_0)y - z_0y') / z'$. As a result, image features in EPIs are distributed along lines with slope $d = (z' + z_0) / z'$ as disparity between associated angles. Such a strong geometric prior provides useful clues for recovering missing information, particularly in the presence of severe degradation.

Specifically, as shown in Fig 4(b), for an unknown depth z , all possible pixels capturing the same 3D position form an "X" shape. To leverage these geometric structures, we propose a transformer structure, named EPIXformer, by constraining its operational searching region to the "X"-shape areas. The structure of EPIXformer is shown in Fig. 4(a). Taking the horizontal EPIXformer as an example, it takes pixel-level features as token $T \in \mathbb{R}^{U \times V \times C}$ to generate query \mathcal{Q} , key \mathcal{K} , and value \mathcal{V} as follows.

$$\begin{aligned} \mathcal{V} &= T \\ \mathcal{Q} &= \mathcal{K} = \text{LayerNorm}(T). \end{aligned} \quad (6)$$

Denote by N_H the number of heads. We split C channels into N_H groups to perform multi-head self-attentions [36]. For each head, EPIXformer constrains the search window of \mathcal{Q} based on Eq. (5). Since the slopes of linear structures in EPIs are unknown in real scenarios, we propose using an X-

shape search window that adapts to possible depth in a wide range.

Specifically, denote by H the output of a particular head, and by W_q , W_k , and W_v the learnable matrices of multiplication projection weights for query \mathcal{Q} , key \mathcal{K} , and value \mathcal{V} , respectively. The transformer of the h^{th} head is described as

$$\begin{aligned} H &= X \mathcal{V} W_v, \\ X &= \text{Softmax} \left(\frac{\mathcal{Q} W_q (\mathcal{K} W_k)^T}{\sqrt{C/N_H}} + M \right), \end{aligned} \quad (7)$$

where M is the mask to constrain the operational regions defined as

$$M(v_q, y_q, v_k, y_k) = \begin{cases} 0, & \text{if } \left| \frac{y_k - y_q}{v_k - v_q} \right| \leq d_{\max}, \\ -\infty, & \text{otherwise.} \end{cases} \quad (8)$$

In Eq. (8), y_k and v_k (y_q and v_q) are indices for the key (query) matrix, and d_{\max} is maximum disparity depending LF task configuration (detailed in Sec. IV-C).

Denote by $\mathcal{H} = [H_1, H_2, \dots, H_{N_H}]$ the concatenation of all heads. The output feature of all the heads is $\mathcal{H} W_O$, where W_O is the learnable multiplication projection matrix. The output of the MHXA block is obtained by using a residual update strategy $T := \mathcal{H} W_O + T$ as shown in Fig 4(a).

With the proposed MHXA block, the constructed transformer (XT) is shown in Fig 5(d). As shown in Fig. 5(c), the overall transformer structure, named *EPIXformer*, operates XT twice successively on horizontal and vertical EPI subspaces to exploit the geometric correlation. The feature is finally converted to the SAI domain to have the same shape as its input.

C. Network Architecture

The overall network architecture is shown in Fig. 5. To learn the ensemble representation of C_4^2 LF subspaces, we cascade the six subspace-specific feature extractors with 64 channels

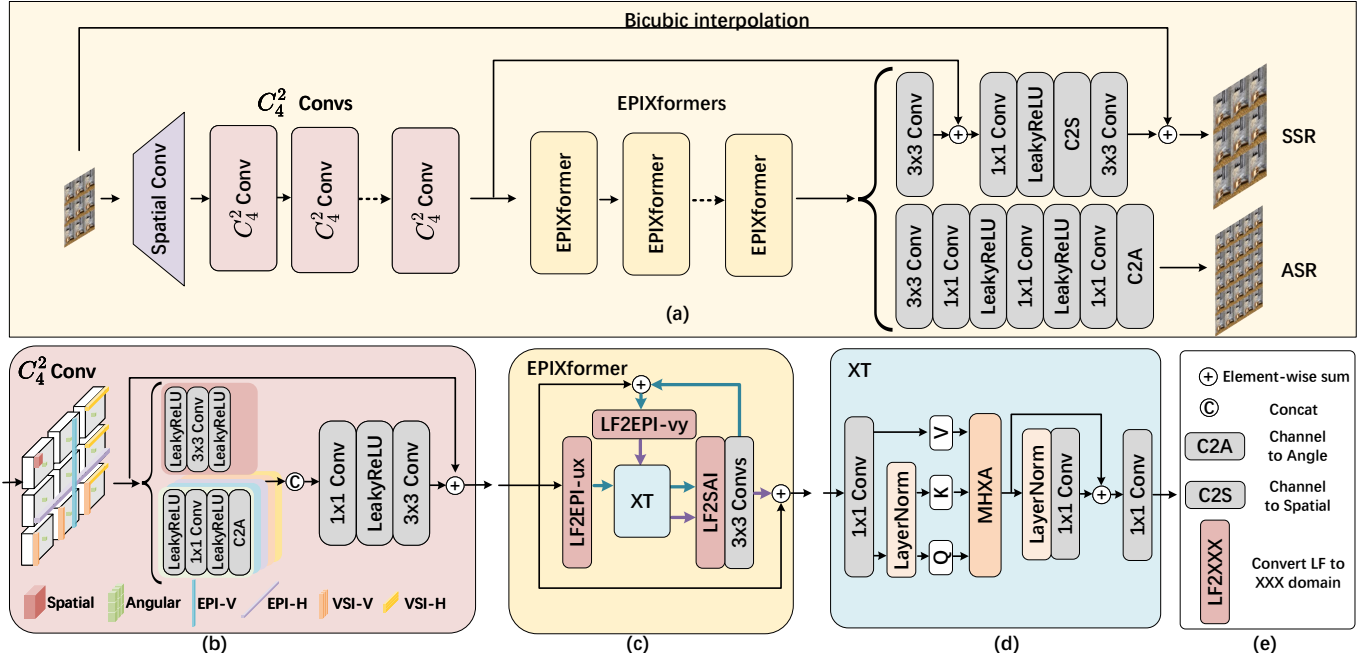


Fig. 5. Overview of proposed spatial and angular super-resolution networks.

after a 3×3 spatial convolution. Then, six EPIXformers are subsequently followed to equip the model with geometry-aware decoding capacity. Finally, we rearrange channel dimension to spatial or angular dimension to have the target size. Specifically, for the SSR task, we use a simple convolution and shuffle net to recover the pixel numbers. For the ASR, we follow Ref. [8, 33] to achieve angular SR on macro-pixels, which recovers the angular resolution by shuffling on the MacPI subspace.

V. EXPERIMENTS AND RESULTS

A. Settings

For spatial SR, we follow previous works [8, 21, 44] to use 5 public LF datasets (*i.e.*, *EPFL* [46], *HCInew* [47], *HCIold* [48], *INRIA* [49], *STFGantry* [50]) for both training and testing. We extracted the central 5×5 views in each LF image, which were cropped into patches with spatial size of 64×64 for $\times 2$ SR and 128×128 for $\times 4$ SR. For each pair, we first convert RGB into YCbCr, then use the Y channel for training or test. We get the LR images resized from the HR ones using bicubic interpolation. The parameter d_{\max} of the mask in Eq. (8) is set to 2 pixels for SSR since the maximum disparity of ground-truth LF dataset is about 3 pixels for these datasets and the disparities of the input LF images are further reduced due to the spatial downsampling.

For angular SR, we perform experiments on both real-world and synthetic scenes. We follow previous work to utilize the 100 real-world scenes captured by Lytro Illum from Stanford Lytro Archive [50] and Kalantari *et al.* [51] to train the network. The real-world test sets are composed of *Occlusion* and *Reflective* splits of Stanford Lytro Archive and *30scenes* from [51]. For synthetic scenes, 20 scenes for HCInew datasets [47] are utilized as training data. As for the

test data, 4 scenes from HCInew [47] and 5 scenes from HCIold [52] are adopted. In this work, we focus on the $2 \times 2 \rightarrow 7 \times 7$ task, since the selected 2×2 SAIs are located at the corner of a 7×7 SAI array, which means that the angular sampling stride is 6 angles, so the angular upsampling factor $\beta = 6$. To generate the training and testing pairs, we follow previous works [8, 23, 24, 29, 33] to sample the sparse views from the ground-truth LF images. For ASR, the parameter d_{\max} of the mask in Eq. (8) is set to 6 (18) pixels for real (synthetic) datasets because the maximum disparity of real (synthetic) datasets is about 1 (3) pixels and the disparities in the input LF images are enlarged due to the angular downsampling with a stride of 6 angles.

The data augmentation strategies we use are random horizontally flipping, vertically flipping, 90° rotation. The networks were trained using L_1 Loss, optimized using Adam [53] optimizer ($\beta_1 = 0.9, \beta_2 = 0.999$) with a start learning rate 2×10^{-4} which halved every 15 epochs. The training was stopped after 80 epochs. The batch size we use is 8/4 for spatial/angular SR.

In the test stage, we reflectively padded the image to deal with the margin region, then cropped the input LF image into patches. Following previous work [8, 21, 44], We calculate the peak signal-to-noise ratio (PSNR) and structural similarity (SSIM) metrics on the Y channel. In detail, we first calculate the metrics for each SAI of each LF image, then average A^2 angles as the PSNR or SSIM for this LF scene (for angular SR, the input SAIs are not used to calculate the metrics), then the PSNR or SSIM of one dataset is the average of all scenes in this test dataset. See our code for more details.

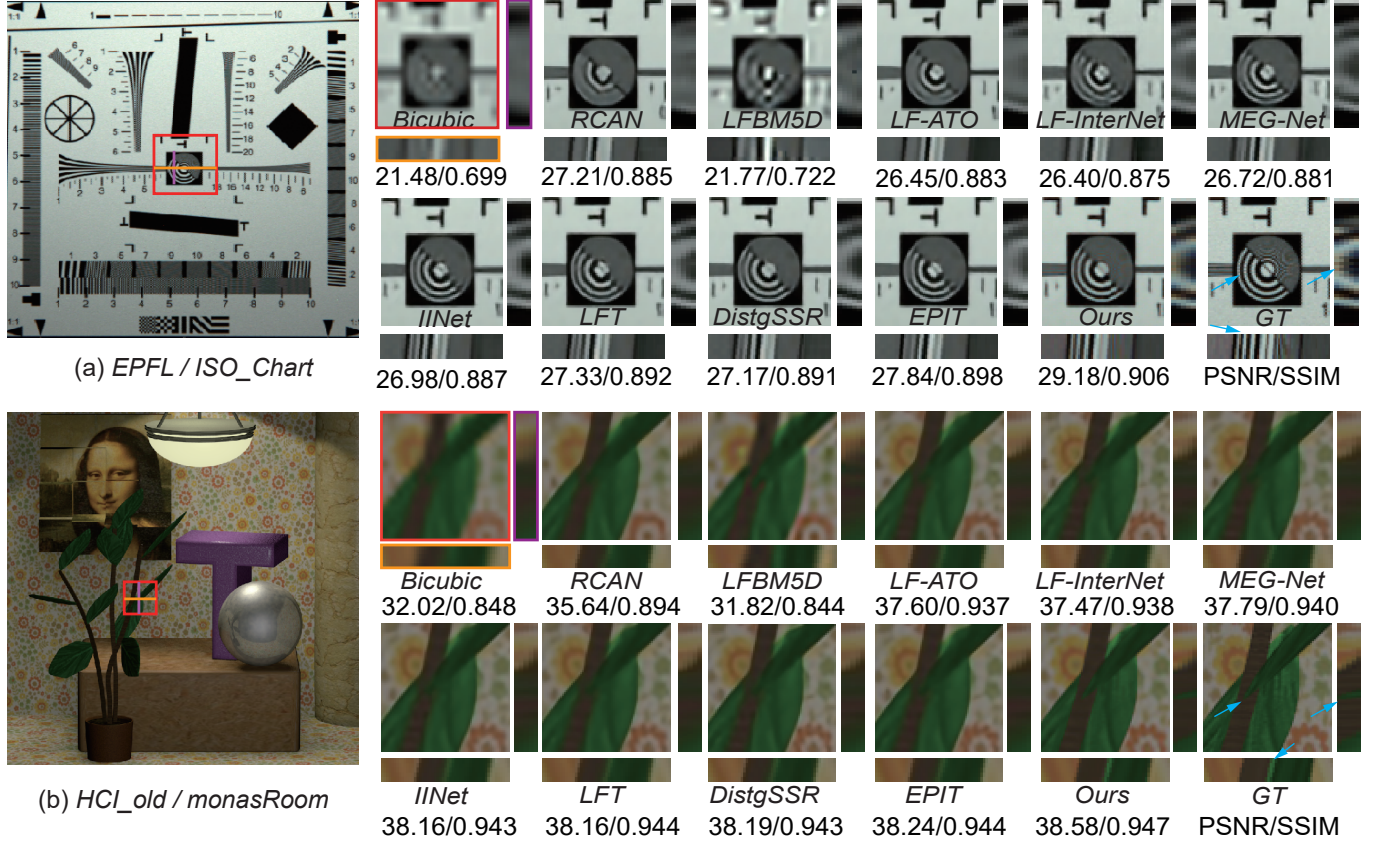


Fig. 6. Visual performance on LF spatial super resolution $\times 4$: (a) The center view (red), the vertical VSI (violet) and the horizontal EPI (orange) of all methods. (b) The center view (red), the vertical VSI (violet) and the horizontal EPI (orange) of all methods.

TABLE I
QUANTITATIVE COMPARISON OF DIFFERENT SR METHODS IN TERMS OF PSNR/SSIM. THE BEST RESULTS ARE SHOWN IN BOLD.

Methods	$\times 2$					$\times 4$				
	EPFL	HCInew	HCIold	INRIA	STFgantry	EPFL	HCInew	HCIold	INRIA	STFgantry
Bicubic	29.74/0.938	31.89/0.936	37.69/0.979	31.33/0.958	31.06/0.950	25.26/0.832	27.71/0.852	32.58/0.934	26.95/0.887	26.09/0.845
VDSR [37]	32.50/0.960	34.37/0.956	40.61/0.987	34.44/0.974	35.54/0.979	27.25/0.878	29.31/0.882	34.81/0.952	29.19/0.920	28.51/0.901
EDSR [38]	33.09/0.963	34.83/0.959	41.01/0.987	34.98/0.976	36.30/0.982	27.83/0.885	29.59/0.887	35.18/0.954	29.66/0.926	28.70/0.907
RCAN [39]	33.16/0.963	35.02/0.960	41.13/0.988	35.05/0.977	36.67/0.983	27.91/0.886	29.69/0.889	35.36/0.955	29.80/0.928	29.02/0.913
LFBM5D [5]	31.15/0.955	33.72/0.955	39.62/0.985	32.85/0.970	33.55/0.972	26.61/0.869	29.13/0.882	34.23/0.951	28.49/0.914	28.30/0.900
resLF [40]	33.62/0.971	36.69/0.974	43.42/0.993	35.40/0.980	38.35/0.990	28.26/0.903	30.72/0.911	36.70/0.968	30.34/0.941	30.19/0.937
LFSSR [41]	33.67/0.974	36.80/0.975	43.81/0.994	35.28/0.983	37.94/0.990	28.60/0.912	30.93/0.914	36.91/0.970	30.59/0.947	30.57/0.943
LF-ATO [16]	34.27/0.976	37.24/0.977	44.20/0.994	36.17/0.984	39.64/0.993	28.51/0.911	30.88/0.913	37.00/0.970	30.71/0.948	30.61/0.943
LF-InterNet [15]	34.11/0.976	37.17/0.976	44.57/0.995	35.83/0.984	38.44/0.991	28.81/0.916	30.96/0.916	37.15/0.972	30.78/0.949	30.36/0.941
LF-DFnet [42]	34.51/0.976	37.42/0.977	44.20/0.994	36.42/0.984	39.43/0.993	28.77/0.916	31.23/0.920	37.32/0.972	30.83/0.950	31.15/0.949
MEG-Net [43]	34.31/0.977	37.42/0.978	44.10/0.994	36.10/0.985	38.77/0.992	28.75/0.916	31.10/0.918	37.29/0.972	30.67/0.949	30.77/0.945
LF-IINet [44]	34.73/0.977	37.77/0.979	44.85/0.995	36.57/0.985	39.89/0.994	29.04/0.919	31.33/0.921	37.62/0.973	31.03/0.952	31.26/0.950
DPT [45]	34.49/0.976	37.35/0.977	44.30/0.994	36.41/0.984	39.43/0.993	28.94/0.917	31.20/0.919	37.41/0.972	30.96/0.950	31.15/0.949
LFT [20]	34.80/0.978	37.84/0.979	44.52/0.995	36.59/0.986	40.51/0.994	29.25/0.921	31.46/0.922	37.63/0.974	31.20/0.952	31.86/0.955
DistgSSR [8]	34.81/0.979	37.96/0.980	44.94/0.995	36.59/0.986	40.40/0.994	28.99/0.919	31.38/0.922	37.56/0.973	30.99/0.952	31.65/0.954
LFSSR-SAV [7]	34.62/0.977	37.42/0.978	44.22/0.994	36.36/0.985	38.69/0.991	29.37/0.922	31.45/0.922	37.50/0.972	31.27/0.953	31.36/0.951
EPIT [21]	34.83/0.978	38.23/0.981	45.08/0.995	36.67/0.985	42.17/0.996	29.34/0.920	31.51/0.923	37.68/0.974	31.37/0.953	32.18/0.957
PILFSSR (Ours)	35.12/0.978	38.51/0.982	45.30/0.995	36.83/0.984	42.22/0.996	30.22/0.924	31.70/0.926	38.04/0.975	32.40/0.954	32.44/0.959

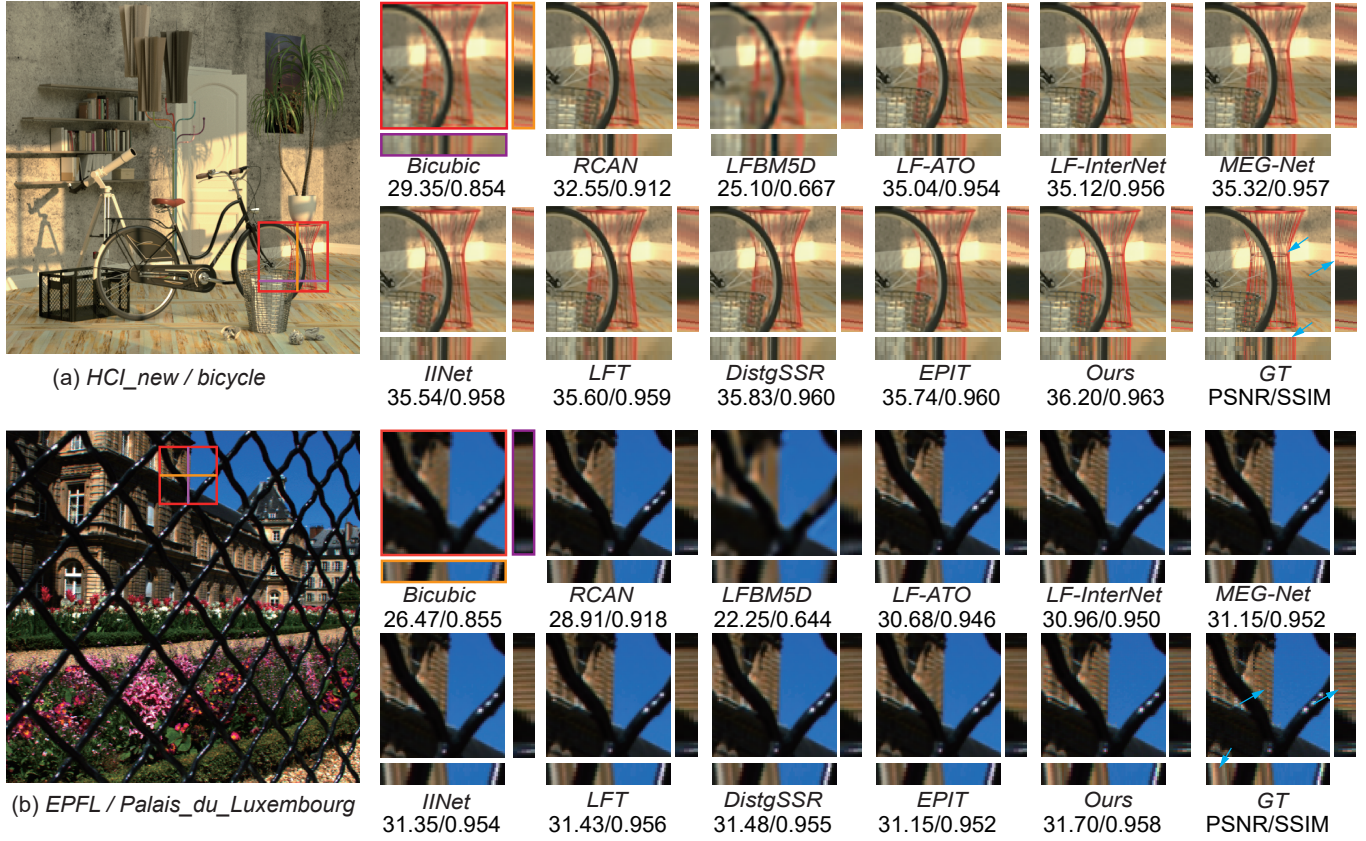


Fig. 7. Visual performance on LF spatial super resolution $\times 2$, the order of these comparing images is the same to $\times 4$: (a) The center view (red), the horizontal VSI (violet) and the vertical EPI (orange) of all methods. (b) The center view (red), the vertical VSI (violet) and the horizontal EPI (orange) of all methods.

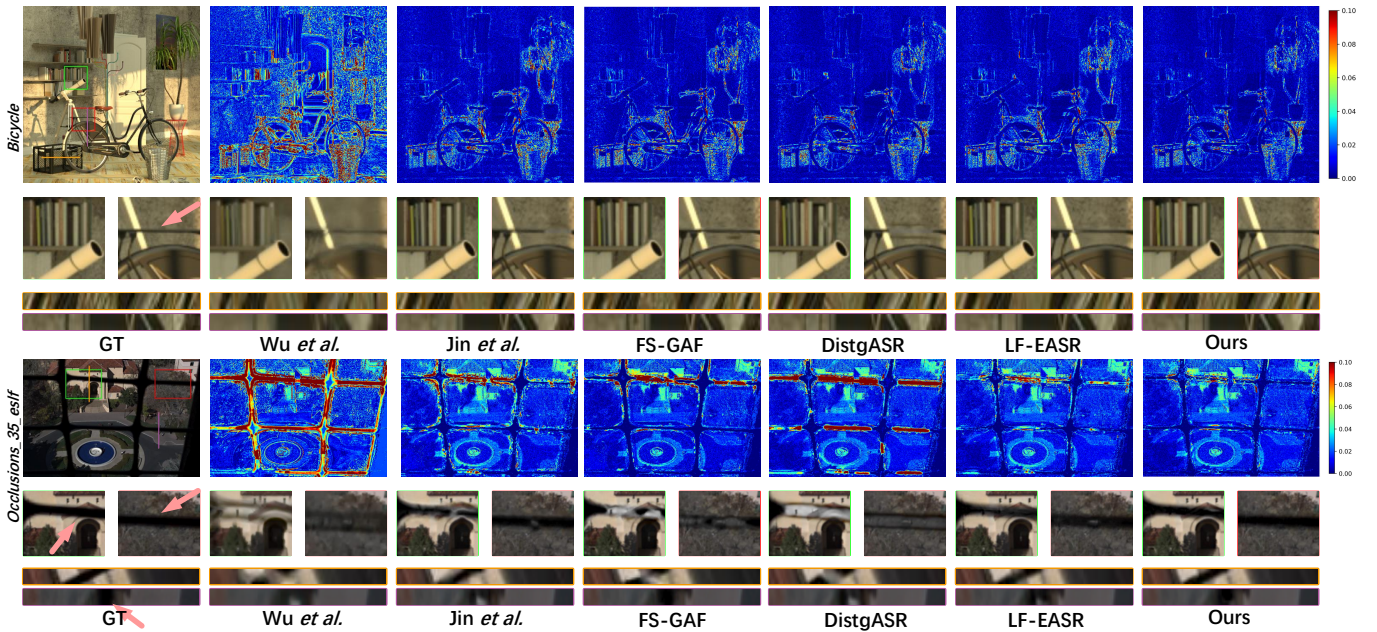


Fig. 8. Visual comparison on real-world scenes for $2 \times 2 \rightarrow 7 \times 7$ task. For comparison, we provide the error maps, enlarged patches highlighted in red and green boxes, and VSI (cutting along the violet line) and EPI (cutting along the orange line) of all methods.

TABLE II

QUANTITATIVE COMPARISONS (PSNR/SSIM) OF THE PROPOSED APPROACH WITH THE STATE-OF-THE-ARTS FOR $2 \times 2 \rightarrow 7 \times 7$ ANGULAR SR. THE BEST RESULTS ARE HIGHLIGHTED IN BOLD AND THE SECOND-BEST RESULTS ARE UNDERLINED.

Datasets	Kalantari <i>et al.</i> [23]	Wu <i>et al.</i> [28]	Yeung <i>et al.</i> [29]	Jin <i>et al.</i> [24]	FS-GAF [25]	DistgASR [8]	LF-EASR [33]	PILFASR (Ours)
<i>30scenes</i>	41.40 / 0.982	33.66 / 0.918	42.77 / 0.986	42.54 / 0.986	42.75 / 0.986	<u>43.67 / 0.989</u>	43.44 / <u>0.989</u>	43.81 / 0.990
<i>Occlusions</i>	37.25 / 0.972	32.72 / 0.924	38.88 / 0.980	38.53 / 0.979	38.51 / 0.979	39.46 / 0.983	<u>39.80 / 0.985</u>	40.18 / 0.986
<i>Reflective</i>	38.09 / 0.953	34.76 / 0.930	38.33 / 0.960	38.46 / 0.959	38.35 / 0.957	39.11 / <u>0.960</u>	<u>39.35 / 0.963</u>	39.61 / 0.963
<i>HCInew</i>	32.85 / 0.909	26.64 / 0.744	32.30 / 0.900	34.60 / 0.937	<u>37.14 / 0.966</u>	35.96 / 0.959	35.86 / 0.956	37.17 / 0.971
<i>HCIold</i>	38.58 / 0.944	31.43 / 0.850	39.69 / 0.941	40.84 / 0.960	41.80 / <u>0.974</u>	<u>42.18 / 0.967</u>	41.54 / 0.960	43.29 / 0.984

B. Quantitative Results

To demonstrate the effectiveness of the proposed method, we compare our spatial SR scheme with 17 other state-of-the-art networks and angular super-resolution scheme with 7 other ones. The previous spatial super-resolution works include five single-image SR methods, *i.e.*, bicubic interpolation, VDSR [37], EDSR [38], and RCAN [39], and 13 LFSSR methods, *i.e.*, LFBM5D [5], resLF [40], LFSSR [41], LF-ATO [16], LF-InterNet [15], LF-DFnet [42], MEG-Net [43], LF-IINet [44], DPT [45], LFT [20], DistgSSR [8], LFSSR-SAV [7], and EPIT [21]. The compared angular SR works include Kalantari *et al.* [23], Wu *et al.* [28], Yeung *et al.* [29], Jin *et al.* [24], FS-GAF [25], DistgASR [8], LF-EASR [33]. For a fair comparison, all the compared methods except angular super-resolution work [28] (the training codes are not publicly available) are trained on the same training datasets as ours.

1) *Results for LFSSR*: For spatial SR, the results are reported in Table I. Compared with the single image SR methods, the performance of LFSSR methods can be highly improved by considering the LF property. By incorporating the physical prior of LF optical imaging, our method achieved state-of-the-art performance for both $\times 2$ and $\times 4$ spatial SR. Compared with 16 previous methods, we can observe that our method has advantages on real-world *EPFL* and *INRIA* test data, which were captured using a Lytro LF camera. Our method outperforms the second-best method EPIT by 0.88 dB on *EPFL* and 1.03 dB on *INRIA* for $\times 4$ SR. That suggests that our method can exploit more information from intrinsic LF prior especially when disparity is very small. Our method also achieves the best performance on synthetic *HCI* and *STFgantry* test data, in which the data have a relatively larger disparity. These demonstrate that our method can also handle LF images with large disparity.

2) *Results for LFASR*: The quantitative comparison results for angular SR are listed in Table II. We can observe that our method achieves state-of-art performance on both real-world and synthetic test sets. Compared with previous methods, for real-world test sets, we can observe that our method outperforms LF-EASR by 0.37 dB on *30scenes* test sets. The EPI based method, Wu *et al.* [28] leads to inferior performance compared with depth and non-depth based methods due to the under-utilized spatial information. The depth-based methods, Kalantari *et al.* [23], Jin *et al.* [24], and FS-GAF [25] struggle to handle small-disparity real-world scenes. As for *Occlusions* and *Reflective* test sets, which contain challenging occluded regions and non-Lambertian surfaces, our method surpasses

the second-best method, LF-EASR [33] by 0.38 dB and 0.26 dB, respectively. For synthetic test sets, our method is the only non-depth based method that outperforms FS-GAF [25] on the *HCInew* test set. Compared with DistgASR [8], Our method also achieves a gain of 1.11 dB on the *HCIold* test set.

3) *Discussion*: The disparity is one of the most important attributes for LF images. For one specific LF data, if the original disparity is at most 4 pixels between every 2 adjacent SAIs, then for $\times 4$ spatial downsampled LF, the disparity is at most $4/4 = 1$ pixel. Similarly, the disparity is at most $4/2 = 2$ pixel for $\times 2$ downsampled one. While for angular SR task, the selected 2×2 SAIs are located at the corner of a 7×7 SAI array, which means that the angular sampling stride is 6 angles and the spatial resolution is not downsampled. Therefore, the disparity will be at most $4 \times 6 = 24$ pixels. By performing the SR task on $\times 4$, $\times 2$ SSR and $\times 6$ ASR, we verified that the proposed method could generalize to LF tasks with a wide range of disparity.

C. Visual Results

In this subsection, we provide visual comparisons for spatial and angular SR tasks.

1) *Results for LFSSR*: Fig 6 and Fig 7 present the visual comparison for $\times 4$ and $\times 2$ spatial SR. In each figure, the zoom-in patches of SAIs, EPIs, and VSIs are highlighted using red, orange, and violet boxes, respectively. From Fig 6 (a), we can observe that our reconstructed image is sharper and have fewer artifacts than other methods. Fig 6 (b) shows an indoor scene, from which we could find that only our method recovered the cusp of the leaves. Fig 7 shows $\times 2$ SR comparison. In Fig 7 (a), from the comparison of a synthetic scene *bicycle*, we can see that the red object reconstructed by our method is clearer, the lines we pointed using arrows are separable while other methods are too blur to distinguish these lines. Fig 7 (b) shows the results on a real scene *Palais_du_Luxembourg*, the color of pointed position on EPI is yellow while other methods appeared gray, and the VSI indicated that our methods recovered more details than others. In summary, we can observe that our results are more distinguishable than that of other methods, and more faithful to ground truth.

2) *Results for LFASR*: The visual comparison results for angular SR are shown in Fig. 8. In terms of the error map, the results of our method show fewer errors in the foreground objects of scenes *Occlusions_35_eslf*. From the enlarged patches, we can observe that our method can reconstruct fine-granular

TABLE III
ADDON TO EXSITING METHODS OPERATED ON $2\times$ SSR TASK

	<i>EPFL</i>	<i>HCnew</i>	<i>HCold</i>	<i>INRIA</i>	<i>STFgantry</i>
DistgSSR [8]	34.81/0.979	37.96/0.980	44.94/0.995	36.59/0.986	40.40/0.994
<i>DistgSSR + VSI</i>	34.89/0.977	37.96/0.980	44.96/0.995	36.75/0.984	40.53/0.994
EPIT [21]	34.83/0.978	38.23/0.981	45.08/0.995	36.67/0.985	42.17/0.996
C_4^2 FE + EPIT	34.98/0.979	38.50/0.981	45.24/0.995	36.75/0.986	42.00/0.996
Ours	35.12/0.978	38.51/0.982	45.30/0.995	36.83/0.984	42.22/0.996

TABLE IV
ABLATION EXPERIMENTS OPERATED ON $2\times$ SSR TASK

C_4^2 FE	EPIXformer	<i>EPFL</i>	<i>HCnew</i>	<i>HCold</i>	<i>INRIA</i>	<i>STFgantry</i>
✓	×	34.44/0.978	37.61/0.978	44.62/0.995	36.33/0.985	39.89/0.993
×	✓	34.92/0.977	38.24/0.981	45.10/0.995	36.67/0.985	42.21/0.996
✓	✓	35.12/0.978	38.51/0.982	45.30/0.995	36.83/0.984	42.22/0.996

details, while the compared methods suffer from obvious artifacts. Our reconstructed EPIs and VSIs show fewer artifacts than compared methods. These demonstrate the effectiveness of our method.

D. Ablation Results

To investigate the improvement brought by C_4^2 feature representations and EPIXformer, we introduced some additional variants. Firstly, some previous works [8, 21] can be viewed as our ablation versions. Secondly, we separately removed them and retrained the rest part of our network to demonstrate the effectiveness of 2 parts.

1) C_4^2 Feature Representation: To verify the effectiveness of our C_4^2 feature representations, we conduct several experiments. First, to show the superiority of our C_4^2 feature extractor over the disentangling block [8], in which the VSI feature representations are not considered, we introduce a variant by adding the VSI convolution of C_4^2 FE to DistgSSR, *i.e.* *DistgSSR + VSI*. As shown in Table III, the variant *DistgSSR + VSI* outperforms DistgSSR by 0.16 dB on *INRIA* dataset. That conforms to previous hypothesis that VSI contains rich sub-pixel information especially when disparity is relatively small, such as the real LF images captured using Lytro camera in *EPFL* and *INRIA*. Second, we add the C_4^2 FE into EPIT to form a variant C_4^2 FE + EPIT, which can also be regarded as removing the “X” of our proposed structure. As shown in Table III, the PSNR is 0.26 dB higher on *HCnew* dataset. Furthermore, we design a variant by removing C_4^2 feature extractor, where only EPIXFormers are deployed. As shown in Table IV, the PSNR values are decreased by about 0.2 dB.

2) EPIXFormer: As shown in Table III, the performance of variant C_4^2 FE + EPIT has demonstrated the influences of EPIXFormer. We further removed all EPIXformers from the proposed structure, as shown in Table IV, the PSNR is dropped by more than 0.5 dB for all test data, especially STFgantry. The reason is that the C_4^2 FE in the proposed network had fewer blocks than the variant *DistgSSR + VSI* thus the performance is limited, but it is still competitive to many convolution-based methods, such as LF-DFNet, MEG-Net, and LF-IINet. If we compare variant *EPIXformer* to *DistgSSR +*

VSI, we can find that the PSNR values are improved by more than 1.0 dB on *STFgantry* test set which has a large disparity. That implies that EPIXformer can help enhance the network’s ability to handle large disparities.

VI. CONCLUSION

In this work, we propose a method to incorporate the optical imaging prior into LF image SR network design. Specifically, the optical imaging process formulation shows two aspects for us: on the whole, LF imaging is 4D imaging with significant 2D constrains, and in detail the LF constrain exhibit an “X” shape if we consider every possibility of depth. Under these descriptions, following the divide-and-conquer philosophy, on the one hand, we complement the VSI subspace to make up the C_4^2 subspaces for LF, and correspondingly a C_4^2 LF feature extractor to cope with the C_4^2 representations 1-by-1. And the proposed VSI contains rich subpixel information especially for LFs with relatively small disparity according to the theoretical analysis as well as experimental results. On the other hand, we designed EPIXformer to enhance the relevant features that capturing information of the same 3D real world position. Experimental results show that our method achieves superior performance in both spatial and angular LF super-resolution tasks. Since our experiments hypothesis that depth information is unknown, so EPIXformer was designed to consider all possibilities. The network can be more delicate if depth information is visible in advance, which may be a solution for future work.

REFERENCES

- [1] H. Sheng, R. Cong, D. Yang, R. Chen, S. Wang, and Z. Cui, “Urbanlf: A comprehensive light field dataset for semantic segmentation of urban scenes,” *IEEE Transactions on Circuits and Systems for Video Technology*, vol. 32, no. 11, pp. 7880–7893, 2022.
- [2] Y. Pan, R. Liu, B. Guan, Q. Du, and Z. Xiong, “Accurate depth extraction method for multiple light-coding-based depth cameras,” *IEEE Transactions on Multimedia*, vol. 19, no. 4, pp. 685–701, 2017.
- [3] K.-T. Ng, Z.-Y. Zhu, C. Wang, S.-C. Chan, and H.-Y. Shum, “A multi-camera approach to image-based rendering and 3-d/multiview display of ancient chinese artifacts,” *IEEE Transactions on Multimedia*, vol. 14, no. 6, pp. 1631–1641, 2012.
- [4] G. Chen, H. Fu, T. Zhou, G. Xiao, K. Fu, Y. Xia, and Y. Zhang, “Fusion-embedding siamese network for light field salient object detection,” *IEEE Transactions on Multimedia*, pp. 1–11, 2023, early access.
- [5] M. Alain and A. Smolic, “Light field super-resolution via lfbm5d sparse coding,” in *2018 25th IEEE International Conference on Image Processing (ICIP)*. IEEE, 2018, pp. 2501–2505.
- [6] Y. Yoon, H.-G. Jeon, D. Yoo, J.-Y. Lee, and I. So Kweon, “Learning a deep convolutional network for light-field image super-resolution,” in *Proceedings of the IEEE international conference on computer vision workshops*, 2015, pp. 24–32.

- [7] Z. Cheng, Y. Liu, and Z. Xiong, "Spatial-angular versatile convolution for light field reconstruction," *IEEE Transactions on Computational Imaging*, vol. 8, pp. 1131–1144, 2022.
- [8] Y. Wang, L. Wang, G. Wu, J. Yang, W. An, J. Yu, and Y. Guo, "Disentangling light fields for super-resolution and disparity estimation," *IEEE Transactions on Pattern Analysis and Machine Intelligence*, vol. 45, no. 1, pp. 425–443, 2022.
- [9] T. E. Bishop and P. Favaro, "The light field camera: Extended depth of field, aliasing, and superresolution," *IEEE Transactions on Pattern Analysis and Machine Intelligence*, vol. 34, no. 5, pp. 972–986, 2012.
- [10] S. Wanner and B. Goldluecke, "Variational light field analysis for disparity estimation and super-resolution," *IEEE Transactions on Pattern Analysis and Machine Intelligence*, vol. 36, no. 3, pp. 606–619, 2014.
- [11] K. Mitra and A. Veeraraghavan, "Light field denoising, light field superresolution and stereo camera based refocussing using a gmm light field patch prior," in *2012 IEEE Computer Society Conference on Computer Vision and Pattern Recognition Workshops*, 2012, pp. 22–28.
- [12] M. Rossi and P. Frossard, "Geometry-consistent light field super-resolution via graph-based regularization," *IEEE Transactions on Image Processing*, vol. 27, no. 9, pp. 4207–4218, 2018.
- [13] Y. Yuan, Z. Cao, and L. Su, "Light-field image superresolution using a combined deep cnn based on epi," *IEEE Signal Processing Letters*, vol. 25, no. 9, pp. 1359–1363, 2018.
- [14] H. W. F. Yeung, J. Hou, X. Chen, J. Chen, Z. Chen, and Y. Y. Chung, "Light field spatial super-resolution using deep efficient spatial-angular separable convolution," *IEEE Transactions on Image Processing*, vol. 28, no. 5, pp. 2319–2330, 2019.
- [15] Y. Wang, L. Wang, J. Yang, W. An, J. Yu, and Y. Guo, "Spatial-angular interaction for light field image super-resolution," in *Computer Vision—ECCV 2020: 16th European Conference, Glasgow, UK, August 23–28, 2020, Proceedings, Part XXIII 16*. Springer, 2020, pp. 290–308.
- [16] J. Jin, J. Hou, J. Chen, and S. Kwong, "Light field spatial super-resolution via deep combinatorial geometry embedding and structural consistency regularization," in *Proceedings of the IEEE/CVF Conference on Computer Vision and Pattern Recognition*, 2020, pp. 2260–2269.
- [17] Z. Cheng, Z. Xiong, and D. Liu, "Light field super-resolution by jointly exploiting internal and external similarities," *IEEE Transactions on Circuits and Systems for Video Technology*, vol. 30, no. 8, pp. 2604–2616, 2020.
- [18] Y. Mo, Y. Wang, C. Xiao, J. Yang, and W. An, "Dense dual-attention network for light field image super-resolution," *IEEE Transactions on Circuits and Systems for Video Technology*, vol. 32, no. 7, pp. 4431–4443, 2022.
- [19] S. Zhou, L. Hu, Y. Wang, Z. Sun, K. Zhang, and X.-q. Jiang, "Aif-lfnet: All-in-focus light field super-resolution method considering the depth-varying defocus," *IEEE Transactions on Circuits and Systems for Video Technology*, pp. 1–1, 2023, early access.
- [20] Z. Liang, Y. Wang, L. Wang, J. Yang, and S. Zhou, "Light field image super-resolution with transformers," *IEEE Signal Processing Letters*, vol. 29, pp. 563–567, 2022.
- [21] Z. Liang, Y. Wang, L. Wang, J. Yang, Z. Shilin, and Y. Guo, "Learning non-local spatial-angular correlation for light field image super-resolution," *arXiv preprint arXiv:2302.08058*, 2023.
- [22] J. Pearson, M. Brookes, and P. L. Dragotti, "Plenoptic layer-based modeling for image based rendering," *IEEE Transactions on Image Processing*, vol. 22, no. 9, pp. 3405–3419, 2013.
- [23] N. K. Kalantari, T.-C. Wang, and R. Ramamoorthi, "Learning-based view synthesis for light field cameras," *ACM Transactions on Graphics (TOG)*, vol. 35, no. 6, pp. 1–10, 2016.
- [24] J. Jin, J. Hou, H. Yuan, and S. Kwong, "Learning light field angular super-resolution via a geometry-aware network," in *Proceedings of the AAAI Conference on Artificial Intelligence*, vol. 34, no. 07, Apr. 2020, pp. 11 141–11 148.
- [25] J. Jin, J. Hou, J. Chen, H. Zeng, S. Kwong, and J. Yu, "Deep coarse-to-fine dense light field reconstruction with flexible sampling and geometry-aware fusion," *IEEE Transactions on Pattern Analysis and Machine Intelligence*, vol. 44, no. 4, pp. 1819–1836, 2022.
- [26] K. Ko, Y. J. Koh, S. Chang, and C.-S. Kim, "Light field super-resolution via adaptive feature remixing," *IEEE Transactions on Image Processing*, vol. 30, pp. 4114–4128, 2021.
- [27] S. Vagharshakyan, R. Bregovic, and A. Gotchev, "Light field reconstruction using shearlet transform," *IEEE Transactions on Pattern Analysis and Machine Intelligence*, vol. 40, no. 1, pp. 133–147, 2018.
- [28] G. Wu, Y. Liu, Q. Dai, and T. Chai, "Learning sheared epi structure for light field reconstruction," *IEEE Transactions on Image Processing*, vol. 28, no. 7, pp. 3261–3273, 2019.
- [29] H. W. F. Yeung, J. Hou, J. Chen, Y. Y. Chung, and X. Chen, "Fast light field reconstruction with deep coarse-to-fine modeling of spatial-angular clues," in *Proceedings of the European Conference on Computer Vision (ECCV)*, September 2018.
- [30] G. Wu, Y. Liu, L. Fang, and T. Chai, "Revisiting light field rendering with deep anti-aliasing neural network," *IEEE Transactions on Pattern Analysis and Machine Intelligence*, vol. 44, no. 9, pp. 5430–5444, 2022.
- [31] G. Wu, Y. Wang, Y. Liu, L. Fang, and T. Chai, "Spatial-angular attention network for light field reconstruction," *IEEE Transactions on Image Processing*, vol. 30, pp. 8999–9013, 2021.
- [32] H. Sheng, S. Wang, D. Yang, R. Cong, Z. Cui, and R. Chen, "Cross-view recurrence-based self-supervised super-resolution of light field," *IEEE Transactions on Circuits and Systems for Video Technology*, pp. 1–1,

- 2023, early access.
- [33] G. Liu, H. Yue, J. Wu, and J. Yang, “Efficient light field angular super-resolution with sub-aperture feature learning and macro-pixel upsampling,” *IEEE Transactions on Multimedia*, pp. 1–13, 2022, early access.
- [34] R. Ng, “Fourier slice photography,” in *ACM Siggraph 2005 Papers*, 2005, pp. 735–744.
- [35] Y. Wang, Z. Liang, L. Wang, J. Yang, W. An, and Y. Guo, “Learning a degradation-adaptive network for light field image super-resolution,” *arXiv preprint arXiv:2206.06214*, 2022.
- [36] A. Vaswani, N. Shazeer, N. Parmar, J. Uszkoreit, L. Jones, A. N. Gomez, Ł. Kaiser, and I. Polosukhin, “Attention is all you need,” *Advances in neural information processing systems*, vol. 30, 2017.
- [37] J. Kim, J. K. Lee, and K. M. Lee, “Accurate image super-resolution using very deep convolutional networks,” in *Proceedings of the IEEE conference on computer vision and pattern recognition*, 2016, pp. 1646–1654.
- [38] B. Lim, S. Son, H. Kim, S. Nah, and K. Mu Lee, “Enhanced deep residual networks for single image super-resolution,” in *Proceedings of the IEEE conference on computer vision and pattern recognition workshops*, July 2017, pp. 136–144.
- [39] Y. Zhang, K. Li, K. Li, L. Wang, B. Zhong, and Y. Fu, “Image super-resolution using very deep residual channel attention networks,” in *Proceedings of the European conference on computer vision (ECCV)*, 2018, pp. 286–301.
- [40] S. Zhang, Y. Lin, and H. Sheng, “Residual networks for light field image super-resolution,” in *Proceedings of the IEEE/CVF conference on computer vision and pattern recognition*, 2019, pp. 11 046–11 055.
- [41] H. W. F. Yeung, J. Hou, X. Chen, J. Chen, Z. Chen, and Y. Y. Chung, “Light field spatial super-resolution using deep efficient spatial-angular separable convolution,” *IEEE Transactions on Image Processing*, vol. 28, no. 5, pp. 2319–2330, 2018.
- [42] Y. Wang, J. Yang, L. Wang, X. Ying, T. Wu, W. An, and Y. Guo, “Light field image super-resolution using deformable convolution,” *IEEE Transactions on Image Processing*, vol. 30, pp. 1057–1071, 2020.
- [43] S. Zhang, S. Chang, and Y. Lin, “End-to-end light field spatial super-resolution network using multiple epipolar geometry,” *IEEE Transactions on Image Processing*, vol. 30, pp. 5956–5968, 2021.
- [44] G. Liu, H. Yue, J. Wu, and J. Yang, “Intra-inter view interaction network for light field image super-resolution,” *IEEE Transactions on Multimedia*, 2021.
- [45] S. Wang, T. Zhou, Y. Lu, and H. Di, “Detail-preserving transformer for light field image super-resolution,” in *Proceedings of the AAAI Conference on Artificial Intelligence*, vol. 36, no. 3, 2022, pp. 2522–2530.
- [46] M. Rerabek and T. Ebrahimi, “New light field image dataset,” in *8th International Conference on Quality of Multimedia Experience (QoMEX)*, no. CONF, 2016.
- [47] K. Honauer, O. Johannsen, D. Kondermann, and B. Goldluecke, “A dataset and evaluation methodology for depth estimation on 4d light fields,” in *Computer Vision—ACCV 2016: 13th Asian Conference on Computer Vision, Taipei, Taiwan, November 20–24, 2016, Revised Selected Papers, Part III 13*. Springer, 2017, pp. 19–34.
- [48] S. Wanner, S. Meister, and B. Goldlücke, “Datasets and benchmarks for densely sampled 4d light fields,” in *VMV 2013 : Vision Modeling and Visualization*, D. Fellner, Ed. Goslar: Eurographics Association, 2013, pp. 225–226.
- [49] M. Le Pendu, X. Jiang, and C. Guillemot, “Light field inpainting propagation via low rank matrix completion,” *IEEE Transactions on Image Processing*, vol. 27, no. 4, pp. 1981–1993, 2018.
- [50] V. Vaish and A. Adams, “The (new) stanford light field archive, 6 computer graphics laboratory,” 2008.
- [51] N. K. Kalantari, T.-C. Wang, and R. Ramamoorthi, “Learning-based view synthesis for light field cameras,” *ACM Transactions on Graphics (TOG)*, vol. 35, no. 6, pp. 1–10, 2016.
- [52] S. Wanner, S. Meister, and B. Goldluecke, “Datasets and benchmarks for densely sampled 4d light fields.” in *VMV*, vol. 13. Citeseer, 2013, pp. 225–226.
- [53] D. P. Kingma and J. Ba, “Adam: A method for stochastic optimization,” *arXiv preprint arXiv:1412.6980*, 2014.